communications physics

A Nature Portfolio journal

Article

https://doi.org/10.1038/s42005-026-02755-9

Full energy partitioning in 2 μm wavelength laser driven extreme ultraviolet sources

Check for updates

D. J. Engels[1,2,4], F. M. Kohlmeier[1,2,4], Y. Mostafa[1,2], E. J. Salumbides[1], B. W. Slotema[1,2], R. Hoekstra[1,3], J. Sheil[1,2], W. Ubachs[1,2] & O. O. Versolato[1,2]

State-of-the-art nanolithography uses extreme ultraviolet (EUV) radiation at 13.5 nm emitted from tin laser-produced plasma (LPP), driven by a 10.6 μm wavelength CO_2-gas laser, to create the smallest features on semiconductor devices. Advances in solid-state laser technologies have led to the alternative concept of a 2-μm-wavelength-driven LPP as a promising candidate for a more efficient and more powerful EUV source. We present the complete energy partitioning for a 2 μm wavelength-driven LPP, reconstructing the full input laser energy. With ~70 %, most of the energy goes into photons, the largest part of which is emitted in the 5–80 nm wavelength range. Plasma ions contribute ~30 % of the energy, and we find that this fraction decreases as a function of the laser intensity, a key insight in finding pathways to optimize plasma for industrial application. Our results offer insight into the energy partitioning of EUV-emitting plasmas for research and industrial nanolithography alike, and provide a benchmark for plasma light source development.

Modern nanolithography machines use extreme ultraviolet (EUV) light to create the most advanced semiconductor devices. To produce this EUV light, tin microdroplets are first laser-shaped into disk targets[1–6] which are subsequently illuminated with 10.6 μm wavelength pulsed laser light, generating plasma containing highly charged, multiply excited tin ions[7–9]. These ions emit EUV light in the desired ± 1 % 'in-band' region around 13.5 nm that is reflected by the Mo/Si multilayer mirrors used[10–13]. A key performance indicator of these laser-produced plasmas (LPPs) is the conversion efficiency (CE): the ratio of laser energy to in-band EUV energy emitted into the 2π hemisphere covered by a collector mirror. State-of-the-art industrial EUV sources, driven by 10.6 μm CO_2 gas laser technology, have CEs of 5–6 % [3,4,14], with ongoing developments to improve their total EUV output and, with it, the wafer throughput of lithography machines[15].

The concept of an LPP driven by 2 μm wavelength laser light has gained traction as a promising alternative candidate in the quest for even more efficient and more powerful EUV sources[16–18]. This activity has been fueled by the rapid development of powerful 2 μm solid-state laser technology[19–21] with the promise of wall-plug efficiencies much higher than CO_2 systems, and pioneering LPP experiments using 2 μm lasers[16,22]. These experiments showed that competitive CE values of up to ~4.5 % can be achieved in a 2 μm-driven system when using a disk target[22]. Radiation hydrodynamic simulations furthermore hinted at the viability of EUV sources driven by 2 μm light without the need to first create a disk target[23], which would strongly simplify the system when suitable long-pulse lasers would become available. No direct experimental evidence is yet available on achieving the predicted[23] high CE values from small droplets under such conditions. Prior experiments on preformed targets, in a double-pulse setting, achieved lower CE values of ~2 % for combinations of target sizes and laser spot sizes similar to the simulation works[22]; the crucial difference being the degree of homogeneity in the spatial intensity distribution of the laser pulse, as explored experimentally previously[22], as well as a dissimilarity in pulse length.

Conversion efficiency, however, is only one figure of merit for EUV-emitting plasmas. A holistic view of all relevant channels distributing the energy of an LPP (see Fig. 1) is required to assess the applicability of new source concepts to EUV lithography. Previous studies have investigated the quantity or anisotropy of EUV emission, key to obtaining reliable CE values, specifically for plasmas driven by 2 μm lasers[16,17,22,24] and other drive laser wavelengths[25–47]. Many studies have focused on the emission spectra of tin plasmas in general, identifying charge states and other features prominent in radiative emissions to understand the origins of EUV emission[13,48–61] or quantifying photon yields in a wide range of wavelength bands[62–70]. The kinetic energy, number, and anisotropy of ions emitted from the plasma[71–84] and their interaction with the plasma surroundings[84–92] have also been

[1]Advanced Research Center for Nanolithography, Amsterdam, The Netherlands. [2]Department of Physics and Astronomy and LaserLab, Vrije Universiteit Amsterdam, Amsterdam, The Netherlands. [3]Zernike Institute for Advanced Materials, University of Groningen, Groningen, The Netherlands. [4]These authors contributed equally: D. J. Engels, F. M. Kohlmeier. e-mail: versolato@arcnl.nl

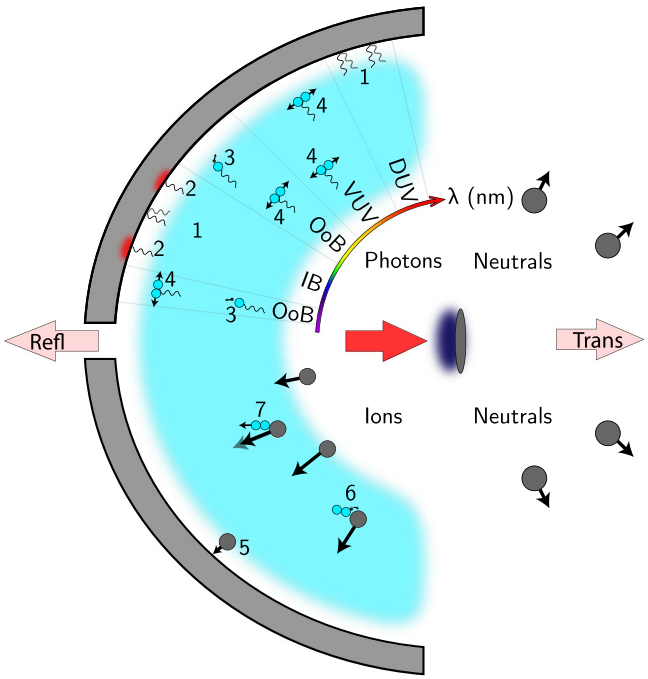


Fig. 1 | Schematic of an industrial laser-produced plasma extreme ultraviolet (EUV) source and its energy partitioning channels. A preformed tin disk is illuminated with a high-energy ns-laser pulse (red, can also transmit or reflect) to generate plasma. Photons and ions, each of a wide range of energies, interact with the surrounding hydrogen buffer gas (blue) and, if not mitigated, the collector mirror. Finally, neutral tin can also be left over after the plasma extinguishes. The numbered processes indicate the various interaction channels.

studied in detail; such studies are key to designing effective mitigation strategies (which typically involve a H_2 buffer gas) to avoid ion-induced damages.

Yet, in spite of the importance of a holistic view, there are no experimental studies available in the public literature that quantitatively combine all of the above channels. In this work, we quantify the *full* energy partitioning for 2 µm wavelength-driven laser-produced plasmas. The independently measured total energy of the dissipation channels matches the input laser energy over a wide range of drive laser intensities. Thus, a complete picture of the output of an EUV-emitting plasma is obtained.

Results

The experiment is described in detail in Methods with the main elements summarized here. We create a tin disk in a vacuum environment from a tin droplet using a laser pre-pulse[1,2,93]. This tin disk is illuminated with a 2 µm main pulse to create an EUV-emitting plasma, cf. Fig. 1. The main pulse originates from a laser system[94] producing high-energy pulses to enable exploratory lab scale experiments at 10 Hz repetition rate, well below that of industrial levels at several 10 kHz. We further note that our setup does not include buffer gas or a collector mirror. For homogeneous heating of the plasma, optimizing CE, the main pulse has a temporal box-shape, and its spatial flat top is imaged onto the disk target[22,23]. The various types of emission from the plasma are measured by absolutely calibrated in-band EUV diodes, a spectrometer, and a set of ion diagnostics mounted to the vacuum chamber. Additionally, we capture the experiment with shadowgraphic imaging and measure the laser profile, reflection, and transmission with 2 µm-sensitive photodiodes.

Plasma photons

Emitted photons affect the surroundings of the plasma and interact in the EUV lithography machine in different ways. The in-band radiation window used in EUV lithography (IB, 13.5 nm ± 1 %) is set by the reflection bandwidth of the multilayer mirror (Fig. 1 process 1). Since $\gtrsim$ 30 % of these IB photons is absorbed by the mirror[95], they may reduce the performance of the multilayer mirrors via heating or deformation (process 2)[96,97]. The surrounding out-of-band EUV photons (OoB, 5–80 nm, excluding IB) interact with the H_2 buffer gas, that embeds the LPP under industrial operating conditions, via photoionization and photodissociation (processes 3 and 4)[98] to form a secondary hydrogen plasma, which can affect nearby optics[99]. Vacuum ultraviolet (VUV, 80–130 nm) radiation is absorbed by the H_2 gas inducing photodissociation (process 4) but has photon energies below the ionization threshold of H_2[98] and does not contribute to direct secondary plasma formation. Finally, deep ultraviolet (DUV, 130–265 nm) can in fact be reflected by the multilayer optics (process 1) towards the wafer and affect the contrast of the exposure in the nanolithographic process[8,69]; the upper limit (265 nm) here is set by our spectrometer.

Figure 2a shows 5–265 nm emission spectra for three (of seven measured) main pulse laser intensities: 2×10^{10} W/cm^2, 6×10^{10} W/cm^2, and 26×10^{10} W/cm^2. Each spectrum is normalized to the area under the curve to highlight the shift of the emission spectrum to shorter wavelengths with increasing laser intensity. Figure 2b zooms in on the 13.5 nm in-band region. It is immediately visible that in-band 13.5 nm radiation is strongest for the 6×10^{10} W/cm^2 intensity case. Three additional features are noted (and are labeled accordingly in Fig. 2b). First (1) are well-defined peak structures between 7 and 10 nm for the two highest intensities. These structures originate from highly charged tin ions of charge states Sn^{12+}–Sn^{15+} [59]. They become more pronounced at the highest laser intensity shown, where additional line structures (associated with charge states beyond Sn^{15+}) also appear at the shortest wavelengths. Second (2) is a shoulder to the main emission peak around 15 nm that is due to the emission by Sn^{7+}, and thus is only prominent until the laser intensity reaches the optimum[58]. Third (3) is a small peak at 17.5 nm that is associated with Sn^{6+} and is only visible at very low drive laser intensities[40,61].

We next quantitatively study the evolution of the charge states z (the average of which $\bar{z}$ scales with the plasma temperature T as $\bar{z} \propto T^{0.6}$ in laser-driven tin plasmas[91,100,101]) of the emitting Sn ions as a function of the laser intensity. We do this by fitting individual emission features in the 7-11 nm range using a method introduced by Torretti et al.[59]. This approach to obtain a plasma temperature yields a power law scaling of the plasma temperature T with laser intensity as $T \propto I^{0.3(1)}$, somewhat weaker than the $T_e \propto I^{0.44-0.6}$ scaling found from modeling laser irradiation of spherical and planar targets[100,102,103] and more in line with Torretti et al., who found $T \propto I^{0.2}$ for a plasma driven by a CO_2 laser. We hypothesize, following Torretti et al., that the weaker-than-expected scaling may reflect the limited validity of using a single temperature in describing a complex evolving plasma that is not perfectly homogeneously heated.

Such single-temperature models, which strongly simplify the reality of a multi-component plasma, have however brought valuable insights and have been shown to enable the reproduction of EUV spectra (see, e.g., Torretti et al.[13] who combined a single-temperature with most comprehensive atomic structure calculations, and Schupp et al.[41] who demonstrated a scaling of a wide range of LPP EUV spectra using an effective optical depth as a single parameter) and aspects of ion emission (see Sheil et al.[91] on the scaling relating of the average charge state and kinetic energy in expand LPPs as well as the broad comparison work of Sheil et al.[101], e.g., on ionization fractions) to a high level of accuracy and in agreement with full scale radiation-hydrodynamics modeling. On the other hand, we also note that the aforementioned models do not take into account the radiative loss fraction[100] that changes with the laser intensity. Regardless, the weak scaling supports a steady performance in terms of the emission of in-band radiation over a wide range of intensities.

The anisotropy of the in-band EUV emission is shown in Fig. 2c. The data points for the individual EUV diodes, and the results of a fit to the data, are normalized to their respective maxima. The emission is strongly anisotropic, relatively close to Lambert's cosine law (which describes the angular emission of a diffuse planar emitter), and this anisotropy does not change with the drive laser intensity.

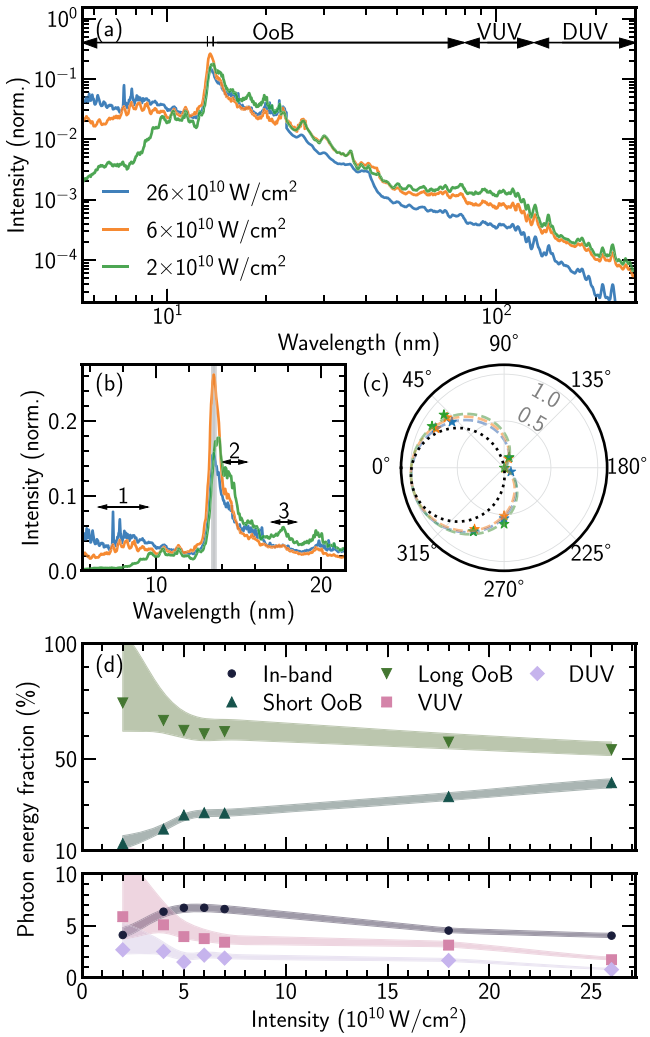


Fig. 2 | Photon energy partitioning. Panel (**a**) shows the full spectrum 5–265 nm for three laser intensities. Each spectrum is normalized to have a constant area under the curve. Panel (**b**) shows a zoom-in on the 13.5 nm in-band region for the same three laser intensities, with three features highlighted (see main text). The in-band region is denoted in gray. Panel (**c**) shows the anisotropic emission of the in-band EUV (extreme ultraviolet) light as measured by EUV-sensitive photodiodes with a cosine function for reference in black (laser incident from left). Panel (**d**) shows the resulting photon energy partitioning, splitting the emissions into in-band EUV (13.5 nm ± 1 %), short out-of-band (short OoB, 5–13.4 nm), long OoB (13.6-80 nm), vacuum ultraviolet (VUV, 80–130 nm), and deep ultraviolet (DUV, 130–265 nm). Shaded bands indicate the systematic uncertainties.

Figure 2d shows the photon energy fractions emitted in the various wavelength bands. The out-of-band is split into short (5–13.4 nm) and long OoB (13.6–80 nm). For each intensity, the values are normalized to the total photon energy across the full wavelength range, highlighting relative changes in emission. Thus, the photon energy fractions sum to 100 %. The uncertainties on the energy fractions are visualized with colored bands. All uncertainties in this work include covariance terms where relevant. The IB peaks at a laser intensity of 6×10^{10} W/cm^2, around the expected optimum intensity for CE, and slowly decreases for higher drive laser intensities[22]. The largest fraction of light is in the OoB range, accounting for more than 80 % of the radiation. The fraction in short OoB increases from 10 % to 40 % when the laser intensity is increased by an order of magnitude, reflecting a higher plasma temperature and with it enhanced emission from the higher charge states. Long OoB emission decreases steadily with increasing intensity, as expected given that line radiation here comes from low charge states whose presence decreases with laser intensity. VUV emission accounts for up to 6 % of the output at the lowest intensity, but is typically around 3 %. DUV emission carries only ~1 % of the total energy emitted in photons. Both VUV and DUV emission fractions reduce for increasing laser intensity. This reduction could be beneficial for exploring pathways that aim to minimize spurious DUV exposure of the wafer.

Plasma ions

Quantifying the ion emission of the plasma is important as ions, the debris of the plasma, are a risk to surrounding diagnostics and optics, especially the collector mirror, which focuses the EUV light and sends it further into the lithography machine. The impact of keV ions would lead to sputtering or implantation (Fig. 1 process 5), degrading mirror performance[104]. To avoid ion impact, the ions are stopped by an H_2 buffer gas. Ions interact with the buffer gas through inelastic (electron capture, molecular fragmentation, process 6)[89,90,92], and elastic (kinetic energy loss, process 7) collisions[87].

Figure 3 shows the kinetic energy distributions of plasma ions for laser intensities ranging between 2 and 26 × 10^{10} W/cm^2. Figure 3a shows the energy spectrum recorded by the ion diagnostic set up at 64° for three different laser intensities (cf. Fig. 2). A wide range of ion energies are present in the spectrum, with a relatively constant contribution between 50 and 500 eV, followed by a drop. The energy position of this drop increases with laser intensity in line with predictions that the kinetic energy of plasma ions (E_{kin}) scales as $E_{kin} \propto \bar{z}T$[105] and thus as $E_{kin} \propto I^{0.5(2)}$ by inserting the previously found scalings. We note that the spectrum is relatively smooth as in refs. 35,71,77,105 and does not feature any peaks such as those prominently observed for 1 µm laser impact on a droplet[81,106]. Differences in wavelength, temporal pulse shape (from Gaussian to box-shaped), as well as geometry of the system could underlie the presence or absence of the ion peak. In addition to the changes in the ion energy distribution, the overall amplitude of the spectrum also increases with laser energy. This follows the expectation since the mass ablation rate (for tin planar targets) was found to scale as $\dot{m} \propto I^{0.6}$[107,108]. The total number of ions detected (integrating over all angles) in our experiment closely matches this scaling, yielding $N_{ion} \propto I^{0.6}$.

In addition to recording overall charge-energy dQ/dE spectra, our ion diagnostics can be used to reconstruct the individual spectra of the contributing charge states. Such a reconstruction is required to be able to assess the total kinetic energy carried by the plasma ions. Figure 3b depicts an example charge-state-resolved spectrum for the 6 × 10^{10} W/cm^2 case. The raw data (dQ/dE) and the reconstructed total charge (with the individual charge states shown separately) agree well. Further comparisons are shown in Fig. 3a where dashed lines depict the total charge from the charge-state-resolved reconstructions. Overall, the reconstructed total charge is in agreement with the raw data, highlighting the quality of the reconstruction of the individual spectra. Charge states up to Sn^{7+} are shown; small amounts of up to Sn^{10+} are included in the reconstruction. Some spikes visible in the spectrum of Sn^{7+} at low energy are artifacts of the analysis procedure; these have negligible contribution to the energy partitioning (note the log scale). Higher charge states become dominant with increasing ion energy[91]. We note that while Sn^{15+} is present in the plasma and its emission lines appear in the photon spectrum, these highly charged tin ions recombine into lower charge states during plasma expansion[86,91,109]. Thus, at the long distances of the detectors from the plasma (~1 m, while charge state freezing already occurs at a distance of several 100 µm [91]), only lower charge states ≤Sn^{10+} are detectable and only in the absence of any buffer gas[89] as in the current case.

Figure 3c shows the anisotropy in the kinetic energy of the plasma ions, normalized to the highest value. Curves interpolating the angularly resolved data are integrated to obtain an angle-integrated kinetic energy of the plasma ions. A dominant fraction of the ions is emitted in the hemisphere on the laser side, similar to the EUV emission but in a much narrower cone – in line with models that predict ions to be emitted predominantly along the surface normal[75,86]. Only in the highest-intensity case is a measurable but still small amount of ions emitted to the back side. This can be explained by the finite thickness of the target, which, with a thickness of 1.5 µm at edge of the beam (the target thickness monotonically decreases outward from the center[110]), is thick enough to sustain the plasma for the full duration of the

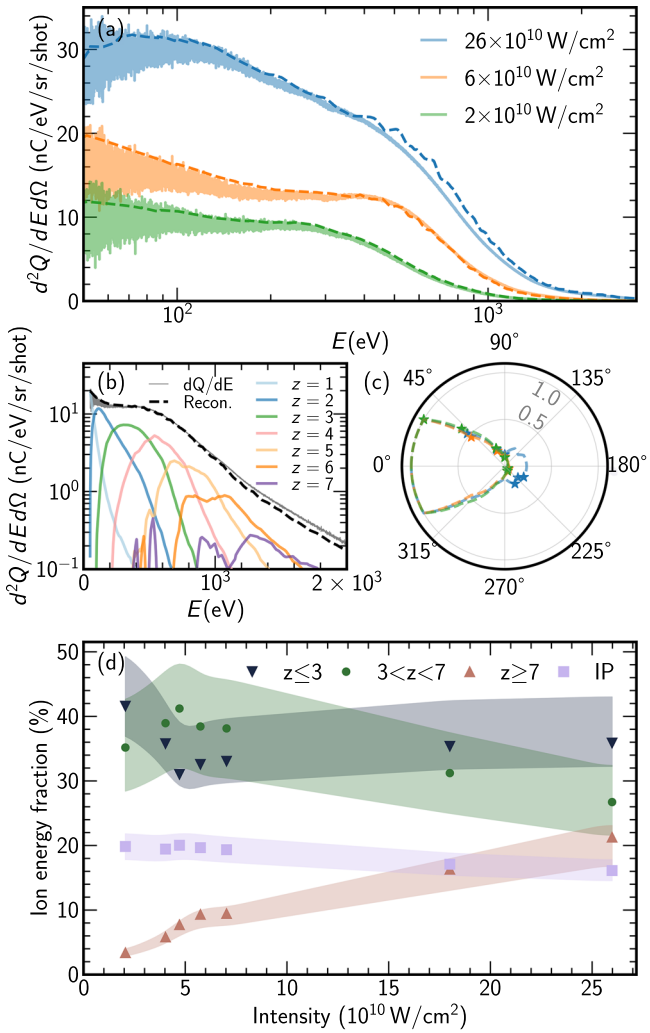


Fig. 3 | Ion energy partitioning. Panel (**a**) shows the kinetic energy spectra at 64° for three different laser intensities. The dashed lines are the result of our ion charge state reconstruction, the transparent traces show the raw Faraday-cup traces. Panel (**b**) zooms in on the ion charge state reconstruction performed for the 6×10^{10} W/cm^2 case at 64° compared to the overall charge-energy dQ/dE spectrum measured. Panel (**c**) shows the anisotropy of the ion emission as recorded by the seven ion diagnostics and the interpolating curve. Panel (**d**) shows the resulting ion energy partitioning. Four different components are shown: the first three are different charge state ranges, while the fourth is the potential energy carried by the ions (sum of sequential ionization energies, IP). Shaded regions indicate the systematic uncertainties.

laser pulse. At the highest laser intensities, however, the plasma is close to, but not yet, using up all the tin in the disk, and some ion emission starts appearing beyond a 90° angle relative to the laser. We again state that the sheet targets are, by design, thick enough to not be mass limited and, thus, sufficient mass is available to sustain the steep density gradient near the critical surface[100] throughout the laser pulse. These findings on not being mass limited are consistent with prior work by Mostafa et al. [111], which indicates, assuming linear scaling of mass use with laser pulse duration and intensity scaling $\sim I^{5/9}$ (following ref. 108) that a overlap mass of 1.1×10^{-14} m^3 would be required to avoid mass limited operation, approximately five times less than the mass available in our experiment with its much larger droplets.

Figure 3d presents the ion energy fractions (again summing to 100 %). Uncertainties are represented by transparent bands. The main change in the ion energy partitioning with laser intensity is the steady increase of the energy carried by the highest charge states, $\geq Sn^{7+}$. As mentioned above, this can be explained by an increased average charge state in the tin plasma, scaling as $\bar{z} \propto I^{0.2(1)}$, while the kinetic energy corresponding to this $\bar{z}$ is known to scale as $E_{kin} \propto \bar{z}^{0.4}$[91]. Thus, the energy fraction carried by the higher charge states increases. In apparent contradiction, the fraction of potential energy carried by the ions remains relatively constant and even slightly decreases with intensity. This behavior can be understood by considering that the number of ions emitted scales as $N_{ion} \propto I^{0.6}$[107,108] and that the total energy to ionize a tin atom to an average charge $\bar{z}$ scales with $\bar{z}^{2.3}$[112]. These scalings are heuristically combined into a scaling of the value of the ionization potential in the energy partitioning $\mathcal{E}_{IP} \propto N_{ion}\bar{z}^{2.3} \propto I^{1.0(1)}$ and thus lead to a constant fraction when expressed as a ratio of the laser intensity (energy).

Energy partitioning

Besides the ions and photons, there are three other small energy channels to be considered: laser reflection, transmission, and kinetic energy carried in neutral tin. We measure laser reflection and transmission using high-speed photodiodes, sensitive to the 2 μm laser wavelength. The experimental data, in accordance with the simulations by Hemminga et al. and de Lange et al.[18,23], indicate that some reflectance, at the percentage level, occurs at early times when the plasma is still in the process of forming. However, accurately determining the absolute value of this reflection is experimentally challenging. Therefore, since the signals show similar evolution in experiments and simulations, we adopt a common 1.5 % reflection value for all intensities, following simulations underlying previous work[18,23]. No laser transmission through or around the target is observed as the sheet targets are designed to be thick enough to prevent mass limitation.

The final energy channel is that of the kinetic energy carried by neutrals in the form of atomic or liquid debris (see Fig. 4a). We conservatively estimate that the neutrals carry at maximum 4 % of the energy at the lower intensities, decreasing to less than 1 % with increasing laser intensity mainly due to a higher ionization degree.

Figure 4b shows the full energy partitioning as a function of laser intensity. We show the total photon emission (a sum of the contributions of all wavelength ranges cf. Fig. 2d), total ion emission (a sum of all contributions cf. Fig. 3d), and the total reconstruction, which also includes the minor contributions from neutrals and reflection (cf. Fig. 4a). For completeness, the in-band emission (part of the photon yield in panel b) is separately shown together with the CE (2π) in the zoom-in at the bottom. These two curves are nearly identical because of the constant anisotropy in the photon emission.

Adding all the contributions, we obtain an average total of 101(14) % with respect to the input laser energy, demonstrating a full reconstruction of the input laser energy.

We observe two main trends. First, CE peaks at 6×10^{10} W/cm^2, around the optimal intensity for EUV generation, and follows the expected behavior throughout the entire intensity range[22]. Underheated plasma cases quickly underperform in terms of CE, while the drop-off in CE with increasing laser intensity is slower. Our CE peaks at 3.5 %, somewhat lower than the ideal 4.5%[22]. However, this CE value is expected for our beam with 66 % of its energy enclosed within the FWHM of the spatial beam profile (cf. Mostafa et al.[22] where the concept of enclosed energy was introduced as a beam quality metric of the top hat for the production of EUV). Second, the balance of photon and ion emission changes as a function of laser intensity, resulting in a decrease of ion emissions from approximately 40 to 25 % in the intensity range studied.

Next, we compare the energy partitioning values with simulations of a 2 μm-driven plasma by Hemminga et al.[18] to validate the predictive power of these simulations performed with a simpler case considering a spherical droplet instead of a disk. They find that 68 % of the energy is converted to radiation and 27 % goes into kinetics at the optimum intensity for CE, as also shown in Fig. 4. Various simulations for spherical and planar targets at similar intensities find ~30–85 % energy in radiation[18,43,113–115]. Previous experiments showed that the radiation output fraction can be as low as 10–20 % from small droplets, also at similar laser intensities as in the current work[40]; this low output fraction is due to incomplete geometric overlap

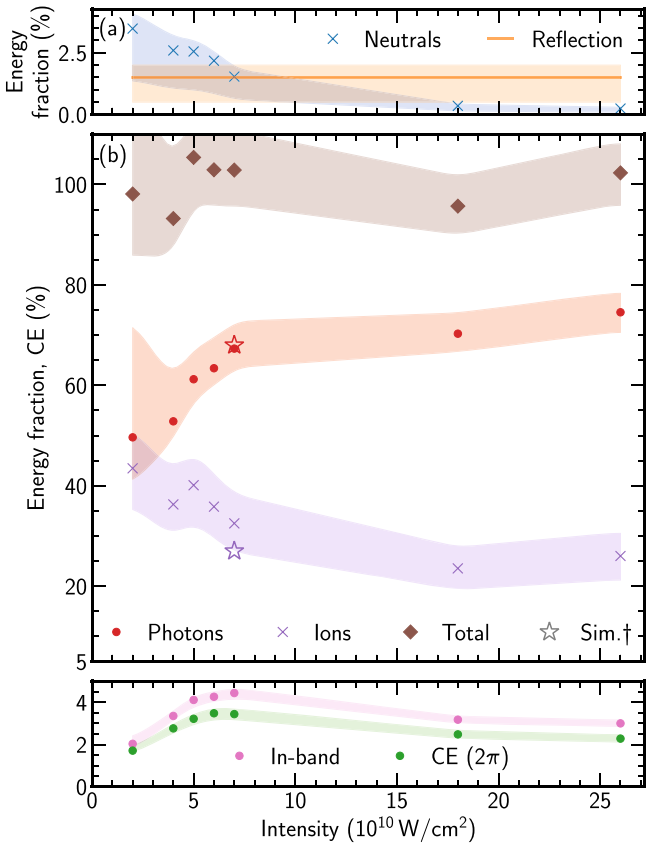


Fig. 4 | Energy partitioning as a function of laser intensity. Panel (**a**) shows contributions of laser reflection and neutrals being propelled by the plasma. Panel (**b**) shows the total energy partitioning shown together with the two main energy channels: ions and photons cf. Figs. 2 and 3. Simulation data points from Hemminga et al.[18] are also shown. The zoom-in panel at the bottom shows the conversion efficiency (CE, 2π) as the typical parameter describing EUV (extreme ultraviolet) producing laser-produced plasma performance together with the total 4π in-band emission. Shaded regions indicate the systematic uncertainties.

between the beam caustic and the much smaller droplet target, a situation dissimilar to the current work. We note that there are significant differences between the various modeling efforts also in terms of the choice of target and laser parameters (including the wavelength), which will impact the outcomes and thus explain the wide range of the obtained radiation output. Around the optimum intensity (6–7 × 10^{10} W/cm^2 in Fig. 4), we find that ~65 % of laser energy is channeled into plasma photons, and ~28 % in ions, which matches the numerical results of Hemminga et al. and falls within the range reported in other works studying different wavelengths and geometries.

Hemminga et al. also studied the dependence of the energy partitioning on the drive laser intensity (over a range similar to ours) considering a 1 µm-driven plasma. They report an almost constant energy partitioning as a function of the laser intensity, in apparent contradiction to our experimental results for a 2 µm-driven system. We can resolve this contradiction when considering the weaker scaling of plasma temperature T uncovered in the current work, which propagates in the expected scaling for the kinetic energy flux density $\mathcal{E}_{\mathrm{Ions}} \propto \rho_s c_s^3 \propto (\bar{z}T)^{3/2} \propto I^{-0.3(2)}$ (with ρ_s the density at the sonic surface, here assumed constant, and the sound speed $c_s \propto \sqrt{\bar{z}T}$[18,116]) consistent with our observations of a decreasing ion load with increasing laser intensity. We separately note that the work of Kawasaki et al.[103] qualitatively sketched expected scalings of the energy partitioning with both pulse length and laser intensity, in line with the current findings.

The complete energy reconstruction demonstrated in the current work provides key input toward industrializing a 2 µm wavelength EUV light source. Moreover, our findings also lead to a consideration of using a laser intensity higher than that leading to optimum CE: overheating the plasma at ~3 × the optimum would lead to a ~30 % reduction of the ion load (although increasing high-energy ion tails cf. Fig. 3, all things being equal, will require further mitigation) and a ~12 % reduction in tin mass consumption per in-band photon (that is, at equal EUV output powers) at the expense of a reduction in CE of ~25 %.

Discussion

We quantify the energy dissipation channels for a 2 µm-driven EUV-emitting light source. The energy of all channels adds up to the input laser energy at all drive laser intensities, with an average deviation of just 1 %. The dominant energy channel is the emission of out-of-band (5–80 nm) light, which carries ~45–70 % of the input energy, increasing with the laser intensity. With increasing light output, the number of atoms required per emitted photon decreases. A weaker-than-expected scaling of plasma temperature with laser intensity, uncovered in the current work, brings our experiments in agreement with pre-existing scaling laws. We note that adherence to any such scaling laws is only validated for the limited range of the current experimental conditions. The second in importance is the fraction of energy channeled into plasma ions, which decreases from ~40 % to 25 % with laser intensity. This finding provides a path for limiting the energy in ions and mass usage, with a relatively small impact on CE. Our findings demonstrate the completeness of our efforts to reconstruct the energy partitioning of a 2 µm-laser-driven plasma light source that is considered as a promising alternative candidate for ever more powerful future EUV sources and provide key input toward industrializing a 2 µm wavelength EUV light source. Moreover, we provide a benchmark for current and future plasma sources of EUV light and provide the required validated toolset for full diagnosis thereof.

Methods

Laser systems & Tin disk creation

We generate a stream of microdroplets by flowing liquid tin through a nozzle within a vacuum chamber at ~10^{-6} mbar, as seen in Fig. 5. The tin microdroplet (diameter 43 µm) is deformed into a disk by a low energy 8 mJ 1 µm pre-pulse, visualized in the inset of Fig. 5. A Spectra-Physics Quanta-Ray Pro-250 Nd:YAG laser produces the 10 ns FWHM pre-pulse. We ensure that our energy partitioning measurements do not include (percentage-level) contributions from the pre-pulse by also taking measurements that include a pre-pulse but no main pulse, which are subsequently subtracted from the data. After a set time (1 µs), the 2 µm main pulse generates an EUV-emitting plasma from the tin disk. At this time delay, the disk is 245 µm in diameter and approximately ~1.5 µm thick (on average)[93], significantly larger than the 85 µm diameter (1/e^2) of the main pulse and thick enough to ensure that the plasma does not run out of tin for the full duration of the main pulse.

We generate the plasma by illuminating a tin disk with a high-intensity master oscillator power amplifier (MOPA) 2 µm main pulse laser[94]. The 2 µm main pulse laser operates at 10 Hz and emits a signal beam with a wavelength of 2080 nm (the idler output is not used)[94]. The laser temporal profile is a uniform box-shape, shaped using a series of Pockels cells. We additionally optimize the spatial profile to be a top hat, which is imaged and demagnified into the vacuum chamber. The energy and intensity I of the main pulse can be changed by a combination of a half-wave plate and a thin-film polarizer. For this work, the pulse length of the laser is kept at 27 ns, where the highest energies, up to 300 mJ, can be produced from the laser system without leading to damage on the amplifier crystals. The energy enclosed within the full width half maximum, E_{encl}, a metric for the quality of the top hat, of the beam is 66 % (cf. Mostafa et al.[22]) typical for the current system.

Diagnostics

A wide range of diagnostics are used to study the generated plasma, as visualized in Fig. 5. Emissions may be anisotropic with the angle α to the laser axis but are rotationally symmetric around the laser axis given the

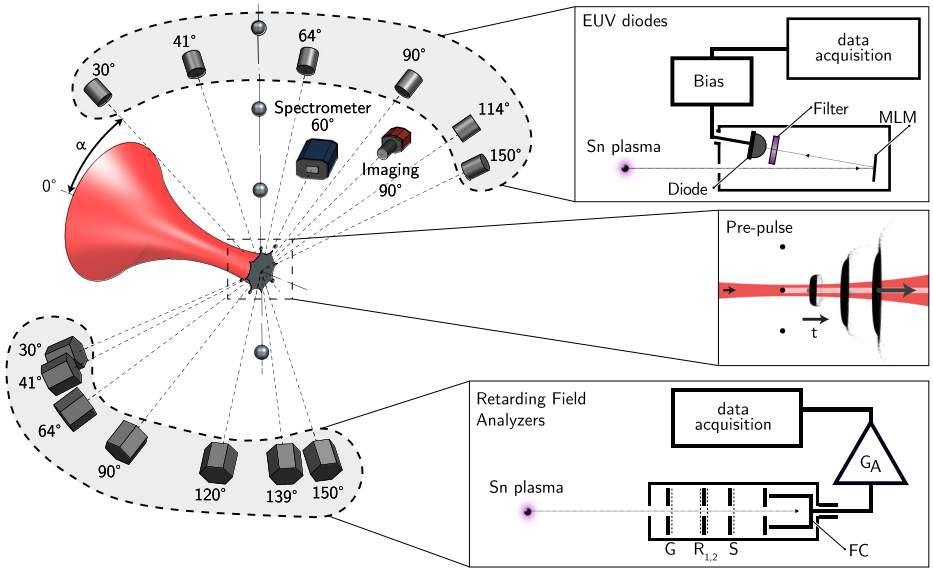


Fig. 5 | Schematic view of the experimental setup. At 0°, the imaged main pulse 2 µm-wavelength laser enters and hits the expanded tin disk. We use a pre-pulse to expand the droplet into a disk over time, as shown in the inset. The six extreme ultraviolet (EUV)-sensitive diodes are shown at the top, with their respective angles to the laser indicated. The inset shows their working principle, with a multi-layer mirror (MLM) reflecting the in-band EUV light onto a photodiode that sits behind a filter. The diode is reverse-biased for faster charge collection. The bottom shows the seven retarding field analyzers (RFAs). Their working principle is shown in an inset as well. The RFAs use four grids: a ground grid, two retarding grids, and a suppressor grid stop the desired ions before the charge is collected in a Faraday Cup. After amplification, the signal is saved and processed. Clustering the detectors on one side is for visualization purposes; they are evenly distributed over both sides and all angles in the actual experiment. The 5–25 nm and 5–265 nm transmission grating spectrometer is at 60°. Finally, the shadowgraphy setup images the experiment using UV light, at 90°, to track the liquid before the main pulse and the liquid and vapor remains after the main pulse. The fast 2 µm-sensitive photodiodes are not shown.

system's symmetry; thus, a single angle (α) describes the location of the various detectors w.r.t. the plasma. We typically capture 100 laser shots for each data point to improve signal-to-noise ratio. The uncertainty in the total reconstructed energy from its components is calculated based on the quadratic sum of the different components given by each diagnostic.

In-band EUV

First, six absolutely calibrated custom in-band-EUV-sensitive photodiodes are placed at angles $\alpha = 30^\circ, 41^\circ, 64^\circ, 90^\circ, 114^\circ$, and 150° to the laser axis. The diode angles, together with their working principle, are also shown in Fig. 5. The diodes are cross-calibrated to a synchrotron-calibrated diode not used in the experiments to avoid any degradation. The EUV in-band emission is calculated separately per diode for each laser shot. The anisotropy function of $E_{\mathrm{IB}}(\alpha) = a + b\cos(\alpha/2)^c$ is fit to the measured EUV values from the photodiodes to obtain the total emission of EUV light, following Schupp et al.[16]. This is converted to a shot-by-shot conversion efficiency (CE) by dividing it by the exact energy for that laser shot. The main source of uncertainty in the in-band EUV measurement comes from the calibration of the EUV diodes. They are calibrated before the experiment, but they degrade slightly in their response (on a percentage level) during the experimental campaign. The total uncertainty in the in-band EUV measurement ranges 5-10 % as visible for the individual diodes in Fig. 2d.

Full emission spectrum

Second, we study the emission spectrum of the plasma using a transmission grating spectrometer[69], placed at 60° to the laser axis. The transmission grating spectrometer has two modes of operation, a high resolution mode (0.11 nm resolution at 13.5 nm) to investigate the 5–25 nm range using a 10,000 lines/mm grating and a wide-range mode to study 5–265 nm using a 1000 lines/mm grating (with 0.8 nm resolution at 13.5 nm)[69]. Sequential exposures, using different filters (selecting from the metallic filters Zr, Si, Al, as well as LiF, MgF_2, UVFS, and four-bounce SiC mirrors) and with exposure times varying between 1 and 500 s, are used to mitigate higher diffraction orders in the measured spectrum. The measured spectra for the different filter combinations are stitched into one full spectrum by correction for filter transmission, diffraction efficiency, and CCD quantum efficiency (cf. Bouza et al.[69]). The spectra of the two diffraction gratings are combined into a single spectrum by first normalizing them to each other with the emissions in their overlapping range. The calibration of the grating's diffraction efficiency limits the fully calibrated spectrum to start at 5 nm on the short-wavelength side (cf. Fig. 2). However, we do extrapolate the known diffraction efficiency down to 1 nm to include an estimate of the 1–5 nm range in the energy partitioning, adding up to 5% at the highest intensities. However, for intensities up to the optimum for CE this contribution is less than 1%. Given the modest heating (to ~30 eV, charge states $\lesssim Sn^{15+}$) we expect and indeed observe only modest emission below 5 nm wavelength in our experiments. We expect that any significant emission below 5 nm would be due to much higher charge states which are not strongly populated in our plasma. Higher laser intensities (beyond those probed in the current work) lead to higher charge states being bred, which would lead to sub-5 nm emission; see, e.g., refs. 117–119. Absolute emission values are obtained by normalizing the single obtained spectrum to the average in-band EUV emission during its ~30 min capture. In calculating the total radiative energy, we assume that the spectrum does not change with the emission angle. Comparing this emission energy to the mean laser energy during the measurement gives a single value for the energy partitioning.

Several sources of uncertainty exist for the full emission spectrum. First, there is uncertainty in the stitching[69] of spectra from various combinations of filters and gratings into one spectrum, which is mitigated by having overlapping regions when stitching. The uncertainty band is estimated from the difference between the spectra in the overlapping regions. Second, uncertainties arise from the quantum efficiency of the CCD, the efficiency of the grating, and the transmissions of the filters as discussed in Bouza et al.[69]. Statistical noise is also factored into the uncertainty calculation, but is typically negligible. Third, an uncertainty arises from the assumption that the emission spectrum does not change with the angle to the laser axis. Explorative RALEF-2D simulations similar to those of Hemminga et al.[106] show that this assumption may lead to an error of by 5–10 % (relative) on the total reconstructed photon emission. Future work could incorporate multiple spectrometers, or multiple photodiodes sensitive to different wavelength bands, to study how the relative emission of wavelengths varies over angle. Combining this uncertainty with the other uncertainties mentioned above yields the error bars as presented in Fig. 2d.

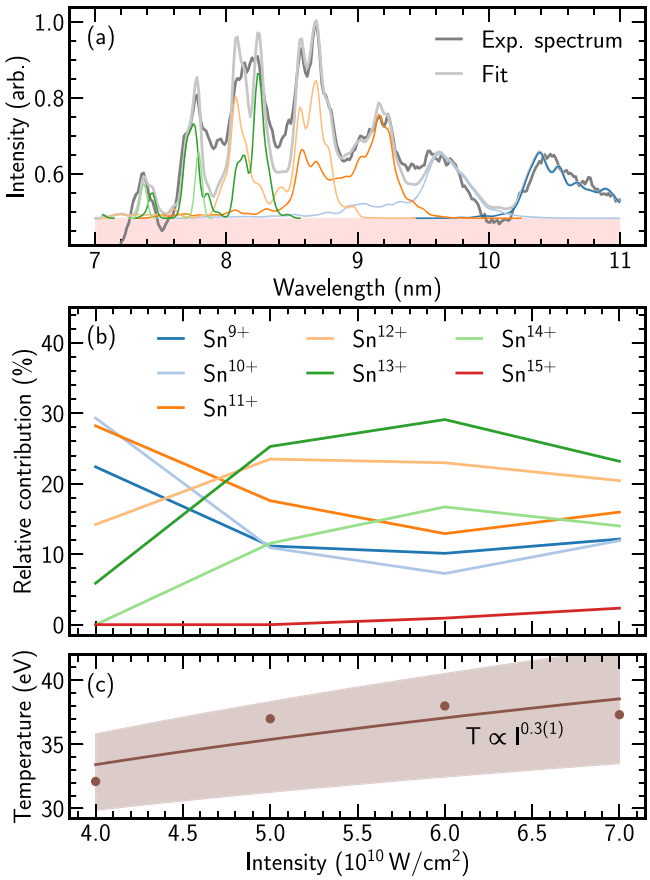


Fig. 6 | Temperature scaling of the plasma. Panel (**a**) shows an example of the fit of the charge-state specific emission peaks to the experimental spectrum at a laser intensity of 6×10^{10} W/cm^2. The underlying charge-state spectra contributing to the fit as well as the constant pedestal are additionally plotted. Panel (**b**) shows the evolution of the different charge states as the laser intensity is increased. Panel (**c**) shows the resulting estimated plasma temperature, together with a power law fit $T \propto I^{0.3(1)}$ with the transparent region indicating the uncertainty interval. The shaded region indicates the systematic uncertainty.

Plasma temperature

To obtain a plasma temperature, separate known spectra of charge states Sn^{9+} to Sn^{15+} are fit to the measured emission spectrum in the range to 7–11 nm where the contributions of the individual charge states can be clearly resolved, following Torretti et al.[59]. An example of the result of this fit to the data is shown in Fig. 6a. In this case and in the others, the model fit captures well over 90 % of the emission. As discussed by Torretti et al., this fitting routine is a robust method to obtain radiation contributions for each charge state. We apply the method to cases with a laser intensity between 4×10^{10} W/cm^2 and 7×10^{10} W/cm^2, which is the intensity regime in which emission lines from Sn^{9+} to Sn^{15+} are dominant. The resulting relative contributions are shown in Fig. 6b. The dependence of the plasma temperature on the laser intensity is deduced, following the methods of Torretti et al., by taking the ratio of the Sn^{12+}/Sn^{13+} contributions and comparing it with calculations from FLYCHK[120]. The result of this method is shown in Fig. 6c and shows a monotonically increasing temperature in this intensity range. The resulting scaling of the temperature with laser intensity at $T \propto I^{0.3(1)}$ is weaker than the values in the literature of 0.44[103] and 0.50[100] more in line (but still above) the weak $T \propto I^{0.2}$ scaling found by Torretti et al. for a CO_2 laser-driven plasma[59]. Several explanations that can affect the relatively weak temperature scaling are discussed in the main text. We note that ionization potential lowering (IPD) here is not expected to significantly impact the charge state balance. Indeed, our calculations based on the work of Ciricosta et al.[121], using both ion-sphere average atom and Stewart-Pyatt formalisms, indicate a modest 5 % reduction of the relevant ionization potentials under the here-relevant plasma conditions.

Plasma ions

The third set of diagnostics comprises seven retarding field analyzers (RFAs, Kimball Physics FC73) ion diagnostics. These RFAs are placed at $\alpha = 30^\circ, 41^\circ, 64^\circ, 90^\circ, 120^\circ, 139^\circ$, and 150° to the laser axis, at a distance of ~1 m from the plasma. Their working principle, including the grids used to stop the ions, is shown in Fig. 5. We incrementally vary the retarding voltage on the RFAs (ranging 0–2 keV) for a total of 60 voltage values, capturing 150 shots for each voltage. These 150 shots are averaged to improve signal-to-noise before the 'bottom-up analysis' is performed to obtain a charge-state-resolved energy spectrum (dN/dE) at each angle (cf. Poirier et al.[80]). These dN/dE spectra are integrated to obtain the energy (or momentum/mass) carried by the individual charge state and by all charge states combined. An anisotropy-corrected absolute energy of ion emission is derived from the combined set of seven RFAs by interpolating between the individual RFAs. Additionally, the ionization energy required to create these ions from neutral tin is calculated by summing over all charge states z, i.e., $\sum_{z=1} \mathrm{IP}_z N_z$, where IP_z is the total energy needed to ionize from neutral tin to that charge state, and N_z is the total number of ions with that charge state[79,112]. While the ions will have had significantly higher charge states within the plasma, any recombination (dominated by the dielectronic recombination process[122]) within the core of the plasma will emit light and thus will be captured by our photon emission diagnostics. Outside of the center 200 μm of the plasma, the charge state is frozen, and thus the ionization energy measured at the RFA in our high-vacuum setup is a metric for the total energy in ionization that has not produced light afterward[86,91,106,109]. Electrons are also emitted by the plasma. However, since the electron and ion (kinetic) temperatures are not so different (nearly thermal) in the plasma[83], around 30 eV, and the ions are 200,000 times more massive, these do not carry any significant kinetic energy. Finally, the obtained values are divided by the mean laser energy during the measurement. This gives a single value for the energy partitioning, just like for the obtained spectra, making the RFA somewhat more sensitive to long-term drifts in laser energy.

The uncertainty in the values obtained by the RFAs originates from four sources. The first uncertainty is due to the transmission of the gridded RFAs. For each RFA, the geometric transmission (averaging at 0.39(4)) is determined via optical inspection of the alignment of the four grids. In addition to geometric transmission, the transmission of the RFA depends on the retarding field applied[123] and may vary on the order of 10 %. Second, the bottom-up[80] reconstruction method introduces potential errors and necessarily relies on simplifications. Some of the uncertainty caused by the bottom-up method is inherent to the method, such as the fact that the multiple isotopes of tin cannot be separated, which reduces the effective resolution. Furthermore, as can be seen in Fig. 3a, some reconstruction cases deviate from the Faraday Cup-like data (that is, RFA data obtained at 0 V retarding voltage). Such deviations may be explained by drifts in laser energy or small changes in laser-to-droplet alignment, visible from the changing RFA reconstruction for RFAs on different sides of the vacuum chamber. Finally, the interpolation over angle, especially the interpolation below 30°, adds uncertainty to the total error bar for ion energies. In total, a 20 % error bar is used as a conservative estimate for any values determined from the ions.

We employ a second method to determine the kinetic energies of the ions to validate the bottom-up RFA reconstruction. This second method is based on a finding by Sheil et al.[91] on a power law scaling for the average charge state as a function of kinetic energy $\bar{z}(E)$, independent of the drive laser intensity. The number of ions N at each energy can be calculated by $dN/dE = dQ/(dEe\bar{z}(E))$, where e is the elementary charge. Following Sheil et al.[91], we define $\bar{z}(E) = 0.3E^{0.4}$, resulting in a simple equation $dN/dE = 2.1 \times 10^{19} dQ/dE \times E^{-0.4}$. This equation shows the advantage of the second method: The obtained dN/dE only depends on the dQ/dE measured at 0 V retarding voltage (Faraday Cup-like). Thus, it is not dependent on the

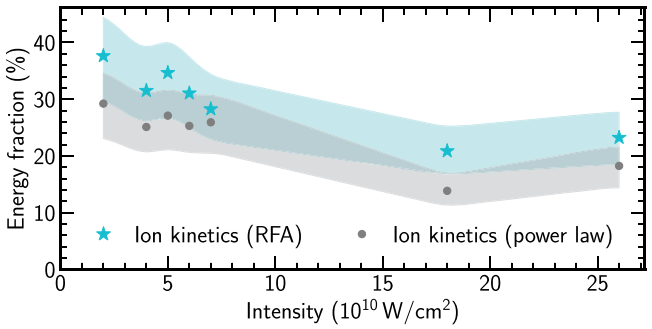


Fig. 7 | Reconstructed ion energy fraction into ion kinetics from two methods. First, the method as shown in Fig. 3. Second, a method based using the power law scaling (see section Plasma ions). Shaded regions indicate the systematic uncertainties.

bottom-up reconstruction method nor is it impacted by drifts during the 30 min RFA scan. However, a similar conservative uncertainty of 20 % is still invoked given the common dependence on the RFA transmission function and the uncertainties related to applying the power law.

Figure 7 compares the ion kinetics as calculated by the RFA method with the $\bar{z}(E)$ power law calculation. The methods show good overall agreement, both qualitatively (showing a decrease over intensity) and quantitatively (in absolute value). The power-law method is consistently slightly below the RFA method, but the difference remains well within the uncertainty estimates.

Neutrals

A fourth diagnostic is spectroscopic shadowgraphic absorption imaging using UV (UV shadowgraphy), which images the tin (before and after the main pulse) at a 90° angle, as can be seen in Fig. 5. We use wavelengths around the 284.08 nm (vacuum wavelength) $5s^25p^2\ ^3P_2$ - $5s^25p6s^3P_2$ neutral tin atomic resonance (cf. Engels et al.[124]) which has the highest possible absorption by neutral tin vapor and enables tracking low-density neutrals leaving the plasma in addition to tracking the liquid before and after the main pulse. The light is generated by a Continuum Horizon OPO and imaged via a single-lens imaging system onto a PCO.ultraviolet camera. Typical velocities of the vapor expansion after laser impact can be observed directly from the shadowgraphy images. This velocity is around 4000 m/s, and the fast neutrals mostly propagate along the laser axis (z). Following Poirier et al. who showed that the neutrals balance the momentum carried by ions for pre-pulse cases[81], we impose that the neutrals post-main pulse should also balance the momentum of the detected ions. Thus, we can combine this momentum obtained with the typical velocity to obtain an estimate of the kinetic energy carried by the neutrals. The results of this method are shown in Fig. 4.

Laser energy, reflection & transmission

We use two 2 µm-sensitive high-speed EOT InGaAs ET-5000 photodiodes to measure laser reflection and transmission. A photodiode at 21° measures reflection from the tin disk, while a photodiode at 180° measures transmitted laser light.

The input laser energy is measured by a calibrated power meter for 2 µm laser light. Such devices carry around 5 % calibration uncertainty. The input laser energy measured in the lab is decreased by the transmission of the final window into the vacuum chamber, which is continuously coated with tin and thus varies during the measurement campaign. This decrease in transmission is carefully quantified, and the input laser energy is corrected for it, without additional significant uncertainty. The quality of the top hat spatial profile of the beam ensures that every position in the beam has sufficient intensity to spark plasma and contribute to the plasma and its emission. Thus, we can state that our input laser energy is not a large source of uncertainty in our energy partitioning, except for the aforementioned 5 % uncertainty due to the externally calibrated power meters.

Data availability

Data underlying the results presented in this paper may be obtained from the authors upon reasonable request.

Received: 14 November 2025; Accepted: 3 July 2026;
Published online: 17 July 2026

References

1. Fomenkov, I. V. et al. Laser produced plasma light source development for HVM. In *Extreme Ultrav. EUV Lithogr. V*, vol. 9048, 755–760 (SPIE, 2014).
2. Schafgans, A. A. et al. Performance optimization of MOPA pre-pulse LPP light source. In *Extreme Ultrav. EUV Lithogr. VI*, vol. 9422, 56–66 (SPIE, 2015).
3. Fomenkov, I. et al. Light sources for high-volume manufacturing EUV lithography: technology, performance, and power scaling. *Adv. Opt. Technol.* **6**, 173–186 (2017).
4. Kouge, K. et al. Update of development progress of the high power LPP-EUV light source using a magnetic field. *J. Photopolym. Sci. Technol.* **33**, 37–44 (2020).
5. Nishimura, Y. et al. Key technology development progress of the high power LPP-EUV light source. In *Opt. EUV Nanolithography XXXV*, vol. 12051, 241–255 (SPIE, 2022).
6. Tomita, K. et al. Observation of plasma inflows in laser-produced Sn plasma and their contribution to extreme-ultraviolet light output enhancement. *Sci. Rep.* **13**, 1825 (2023).
7. Waldrop, M. M. The chips are down for Moore's law. *Nat. N.* **530**, 144 (2016).
8. van de Kerkhof, M. A. et al. High-power EUV lithography: spectral purity and imaging performance. *J. Micro/Nanolithogr. MEMS MOEMS* **19**, 33801 (2020).
9. van Schoot, J. et al. The future of EUV lithography: continuing Moore's law into the next decade. In *Extreme Ultrav. EUV Lithogr. IX*, vol. 10583, 105830R (International Society for Optics and Photonics, 2018).
10. Sasaki, A. et al. Modeling of radiative properties of Sn plasmas for extreme-ultraviolet source. *J. Appl. Phys.* **107**, 113303 (2010).
11. O'Sullivan, G. et al. Spectroscopy of highly charged ions and its relevance to EUV and soft x-ray source development. *J. Phys. B:. Mol. Opt. Phys.* **48**, 144025 (2015).
12. Huang, Q. et al. Spectral tailoring of nanoscale EUV and soft x-ray multilayer optics. *Appl. Phys. Rev.* **4**, 11104 (2017).
13. Torretti, F. et al. Prominent radiative contributions from multiply-excited states in laser-produced tin plasma for nanolithography. *Nat. Commun.* **11**, 2334 (2020).
14. Fomenkov, I., Schafgans, A. & Brandt, D. Laser-produced plasma sources for high-volume-manufacturing EUV lithography. *Synchrotron Radiat. N.* **32**, 3–8 (2019).
15. Zhu, Q. et al. Evolution of EUV light source architecture for continued advancements in EUV high volume manufacturing. In *Opt. EUV Nanolithography XXXVIII*, vol. 13424, 363–369 (SPIE, 2025).
16. Schupp, R. et al. Characterization of angularly resolved EUV emission from 2-μm-wavelength laser-driven Sn plasmas using preformed liquid disk targets. *J. Phys. D: Appl. Phys.* **54**, 365103 (2021).
17. Shi, Z. Y. et al. Enhanced extreme ultraviolet conversion efficiency of a 2 μm laser-driven preformed tin-droplet target using short picosecond pre-pulses. *Phys. Plasmas* **30**, 43107 (2023).
18. Hemminga, D. J., Versolato, O. O. & Sheil, J. Simulations of plasmas driven by laser wavelengths in the 1.064—10.6 μm range for their characterization as future extreme ultraviolet light sources. *Phys. Plasmas* **30**, 33301 (2023).
19. Tamer, I. et al. Demonstration of a compact, multi-Joule, diode-pumped Tm: YLF laser. *Opt. Lett.* **46**, 5096 (2021).
20. Tamer, I. et al. 1 GW peak power and 100 J pulsed operation of a diode-pumped Tm: YLF laser. *Opt. Express* **30**, 46336–46343 (2022).

21. Tamer, I. et al. Demonstration of a 1 TW peak power, joule-level ultrashort Tm: YLF laser. *Opt. Lett.* **49**, 1583–1586 (2024).
22. Mostafa, Y. et al. Erratum: "Production of 13.5 nm light with 5% conversion efficiency from 2 μm laser-driven tin microdroplet plasma" [Appl. Phys. Lett. 123, 234101 (2023)]. *Appl. Phys. Lett.* **126**, 49901 (2025).
23. de Lange, S. J. J. et al. Modeling the hundreds-of-nanoseconds-long irradiation of tin droplets with a 2 μm-wavelength laser for future EUV lithography. *Plasma Sources Sci. Technol.* **33**, 105003 (2024).
24. Yuan, Y. et al. Enhancing the conversion efficiency of extreme ultraviolet light sources using a 2 μm wavelength laser. *Plasma Phys. Controlled Fusion* **64**, 25001 (2021).
25. Fujioka, S. et al. Opacity effect on extreme ultraviolet radiation from laser-produced tin plasmas. *Phys. Rev. Lett.* **95**, 235004 (2005).
26. Shimada, Y. et al. Characterization of extreme ultraviolet emission from laser-produced spherical tin plasma generated with multiple laser beams. *Appl. Phys. Lett.* **86**, 51501 (2005).
27. Ando, T. et al. Optimum laser pulse duration for efficient extreme ultraviolet light generation from laser-produced tin plasmas. *Appl. Phys. Lett.* **89**, 151501 (2006).
28. Higashiguchi, T., Dojyo, N., Hamada, M., Sasaki, W. & Kubodera, S. Low-debris, efficient laser-produced plasma extreme ultraviolet source by use of a regenerative liquid microjet target containing tin dioxide (SnO_2) nanoparticles. *Appl. Phys. Lett.* **88**, 201503 (2006).
29. Fujioka, S. et al. Pure-tin microdroplets irradiated with double laser pulses for efficient and minimum-mass extreme-ultraviolet light source production. *Appl. Phys. Lett.* **92**, 241502 (2008).
30. Morris, O., O'Reilly, F., Dunne, P. & Hayden, P. Angular emission and self-absorption studies of a tin laser produced plasma extreme ultraviolet source between 10 and 18nm. *Appl. Phys. Lett.* **92**, 231503 (2008).
31. Nakamura, D. et al. Ablation dynamics of tin micro-droplet irradiated by double pulse laser used for extreme ultraviolet lithography source. *J. Phys. D: Appl. Phys.* **41**, 245210 (2008).
32. Sequoia, K. L., Tao, Y., Yuspeh, S., Burdt, R. & Tillack, M. S. Two dimensional expansion effects on angular distribution of 13.5nm in-band extreme ultraviolet emission from laser-produced Sn plasma. *Appl. Phys. Lett.* **92**, 221505 (2008).
33. Nishihara, K. et al. Plasma physics and radiation hydrodynamics in developing an extreme ultraviolet light source for lithography. *Phys. Plasmas* **15**, 56708 (2008).
34. Hassanein, A., Sizyuk, T., Sizyuk, V. & Harilal, S. S. Combined effects of prepulsing and target geometry on efficient extreme ultraviolet production from laser produced plasma experiments and modeling. *J. Micro/ Nanolithogr., MEMS MOEMS* **10**, 33002–33002 (2011).
35. Freeman, J. R., Harilal, S. S., Verhoff, B., Hassanein, A. & Rice, B. Laser wavelength dependence on angular emission dynamics of Nd:YAG laser-produced Sn plasmas. *Plasma Sources Sci. Technol.* **21**, 55003 (2012).
36. Giovannini, A. Z. & Abhari, R. S. Three-dimensional extreme ultraviolet emission from a droplet-based laser-produced plasma. *J. Appl. Phys.* **114**, 33303 (2013).
37. Giovannini, A. Z. & Abhari, R. S. Effects of the dynamics of droplet-based laser-produced plasma on angular extreme ultraviolet emission profile. *Appl. Phys. Lett.* **104**, 194104 (2014).
38. Chen, H. et al. Angular distribution of ions and extreme ultraviolet emission in laser-produced tin droplet plasma. *J. Appl. Phys.* **117**, 193302 (2015).
39. Matsukuma, H. et al. Correlation between laser absorption and radiation conversion efficiency in laser produced tin plasma. *Appl. Phys. Lett.* **107**, 121103 (2015).
40. Schupp, R. et al. Efficient generation of extreme ultraviolet light from Nd:YAG-driven microdroplet-tin plasma. *Phys. Rev. Appl.* **12**, 014010 (2019).
41. Schupp, R. et al. Radiation transport and scaling of optical depth in Nd:YAG laser-produced microdroplet-tin plasma. *Appl. Phys. Lett.* **115**, 124101 (2019).
42. Brandstätter, M., Weber, M. M. & Abhari, R. S. Non-axisymmetric droplet irradiation effects on ion and extreme ultraviolet light emission of laser-produced plasma light sources. *J. Appl. Phys.* **129**, 233306 (2021).
43. Sunahara, A., Hassanein, A., Tomita, K., Namba, S. & Higashiguchi, T. Optimization of extreme ultra-violet light emitted from the CO_2 laser-irradiated tin plasmas using 2D radiation hydrodynamic simulations. *Opt. Express* **31**, 31780–31795 (2023).
44. Sizyuk, V., Sizyuk, T. & Hassanein, A. Temporal pre-pulse shaping in dual pulse laser produced plasma for the optimization of the EUV source in tin microdroplet system. *J. Appl. Phys.* **135**, 93101 (2024).
45. Sugiura, T. et al. Efficient extreme ultraviolet emission by multiple laser pulses. *Appl. Phys. Lett.* **125**, 34103 (2024).
46. Wu, Y., Wang, X., Ray, T., Thio, Y. C. F. & Hassanein, A. Experimental study of the dynamics and extreme ultraviolet radiation of laser produced colliding Sn plasmas. *Phys. Plasmas* **31**, 43508 (2024).
47. Wang, T. et al. Characterization of optical depth for laser produced plasma extreme ultraviolet source. *Vacuum* **231**, 113805 (2025).
48. Azarov, V. I. & Joshi, Y. N. Analysis of the $4d^7$-$4d^6$ 5p transition array of the eighth spectrum of tin: Sn VIII. *J. Phys. B:. Mol. Opt. Phys.* **26**, 3495 (1993).
49. Svendsen, W. & O'Sullivan, G. Statistics and characteristics of XUV transition arrays from laser-produced plasmas of the elements tin through iodine. *Phys. Rev. A* **50**, 3710–3718 (1994).
50. Churilov, S. S. & Ryabtsev, A. N. Analyses of the Sn IX–Sn XII spectra in the EUV region. *Phys. Scr.* **73**, 614 (2006).
51. Churilov, S. S. & Ryabtsev, A. N. Analysis of the spectra of In XII–XIV and Sn XIII–XV in the far-VUV region. *Opt. Spectrosc.* **101**, 169–178 (2006).
52. Churilov, S. S. & Ryabtsev, A. N. Analysis of the $4p^64d^7$-$(4p^64d^64f + 4p^54d^8)$ transitions in the Sn VIII spectrum. *Opt. Spectrosc.* **100**, 660–666 (2006).
53. Ryabtsev, A. N., Kononov, ÉY. a & Churilov, S. S. Spectra of rubidium-like Pd X-Sn XIV ions. *Opt. Spectrosc.* **105**, 844–850 (2008).
54. D'Arcy, R. et al. Transitions and the effects of configuration interaction in the spectra of Sn XV–Sn XVIII. *Phys. Rev. A* **79**, 42509 (2009).
55. Ohashi, H. et al. EUV emission spectra in collisions of multiply charged Sn ions with He and Xe. *J. Phys. B:. Mol. Opt. Phys.* **43**, 65204 (2010).
56. Windberger, A. et al. Analysis of the fine structure of Sn^{11+} – Sn^{14+} ions by optical spectroscopy in an electron-beam ion trap. *Phys. Rev. A* **94**, 12506 (2016).
57. Colgan, J. et al. Atomic structure considerations for the low-temperature opacity of Sn. *High. Energy Density Phys.* **23**, 133–137 (2017).
58. Torretti, F. et al. Optical spectroscopy of complex open-4d-shell ions Sn^{7+} – Sn^{10+}. *Phys. Rev. A* **95**, 42503 (2017).
59. Torretti, F. et al. Spectral characterization of an industrial EUV light source for nanolithography. *J. Phys. D: Appl. Phys.* **53**, 55204 (2019).
60. Scheers, J. et al. EUV spectroscopy of highly charged Sn^{13+} - Sn^{15+} ions in an electron-beam ion trap. *Phys. Rev. A* **101**, 062511 (2020).
61. Bouza, Z. et al. EUV spectroscopy of Sn^{5+}–Sn^{10+} ions in an electron beam ion trap and laser-produced plasmas. *J. Phys. B:. Mol. Opt. Phys.* **53**, 195001 (2020).
62. Namba, S. et al. Characterization of out-of-band radiation and plasma parameters in laser-produced Sn plasmas for extreme ultraviolet lithography light sources. *J. Appl. Phys.* **104**, 13305 (2008).
63. Sakaguchi, H. et al. Absolute evaluation of out-of-band radiation from laser-produced tin plasmas for extreme ultraviolet lithography. *Appl. Phys. Lett.* **92**, 111503 (2008).

64. Campos, D., Harilal, S. S. & Hassanein, A. The effect of laser wavelength on emission and particle dynamics of Sn plasma. *J. Appl. Phys.* **108**, 113305 (2010).
65. Gambino, N., Rollinger, B., Hudgins, D. & Abhari, R. S. Spectral emission properties of a laser-produced plasma light source in the sub-200 nm range for wafer inspection applications. *J. Micro/Nanolithogr. MEMS MOEMS* **14**, 34002 (2015).
66. Gambino, N., Rollinger, B., Brandstätter, M. & Abhari, R. S. Vacuum ultraviolet spectral emission properties of Ga, In and Sn droplet-based laser produced plasmas. *Spectrochim. Acta, Part B* **122**, 149–156 (2016).
67. Parchamy, H., Szilagyi, J., Masnavi, M. & Richardson, M. Ultraviolet out-of-band radiation studies in laser tin plasma sources. *J. Appl. Phys.* **122**, 173303 (2017).
68. Scheers, J. et al. Time- and space-resolved optical Stark spectroscopy in the afterglow of laser-produced tin-droplet plasma. *Phys. Rev. E* **102**, 13204 (2020).
69. Bouza, Z. et al. The spectrum of a 1-μm-wavelength-driven tin microdroplet laser-produced plasma source in the 5.5–265.5 nm wavelength range. *AIP Adv.* **11**, 125003 (2021).
70. Pan, Y., Tomita, K., Sunahara, A., Sasaki, A. & Nishihara, K. Joint measurement of electron density, temperature, and emission spectrum of Nd:YAG laser-produced tin plasma. *Appl. Phys. Lett.* **123**, 204103 (2023).
71. Murakami, M., Kang, Y.-G., Nishihara, K., Fujioka, S. & Nishimura, H. Ion energy spectrum of expanding laser-plasma with limited mass. *Phys. Plasmas* **12**, 62706 (2005).
72. Morris, O. et al. Determination of charge state, energy and angular distributions of tin ions emitted from laser produced plasma based EUV sources. *J. Phys. Conf. Ser.* **58**, 391 (2007).
73. O'Connor, A., Morris, O. & Sokell, E. Angular and energy distribution of Sn ion debris ejected from a laser-produced plasma source, for laser power densities in the range suitable for extreme ultraviolet lithography. *J. Appl. Phys.* **109**, 73301 (2011).
74. Giovannini, A. Z., Gambino, N., Rollinger, B. & Abhari, R. S. Angular ion species distribution in droplet-based laser-produced plasmas. *J. Appl. Phys.* **117**, 33302 (2015).
75. Chen, Z., Wang, X., Zuo, D. & Wang, J. Investigation of ion characteristics in CO_2 laser irradiating preformed tin-droplet plasma. *Laser Part. Beams* **34**, 552–561 (2016).
76. Deuzeman, M. J. et al. Ion distribution and ablation depth measurements of a fs-ps laser-irradiated solid tin target. *J. Appl. Phys.* **121**, 103301 (2017).
77. Bayerle, A. et al. Sn ion energy distributions of ns- and ps-laser produced plasmas. *Plasma Sources Sci. Technol.* **27**, 045001 (2018).
78. Brandstätter, M., Gambino, N. & Abhari, R. S. Temporally and spatially resolved ion dynamics of droplet-based laser-produced tin plasmas in lateral expansion direction. *J. Appl. Phys.* **123**, 43308 (2018).
79. Poirier, L. et al. Cross-calibration of a combined electrostatic and time-of-flight analyzer for energy- and charge-state-resolved spectrometry of tin laser-produced plasma. *Appl. Phys. B* **128**, 39 (2022).
80. Poirier, L. et al. Energy- and charge-state-resolved spectrometry of tin laser-produced plasma using a retarding field energy analyzer. *Appl. Phys. B* **128**, 135 (2022).
81. Poirier, L. et al. Strongly anisotropic ion emission in the expansion of Nd:YAG-laser-produced plasma. *Phys. Plasmas* **29**, 123102 (2022).
82. Poirier, L., Lassise, A., Hoekstra, R., Sheil, J. & Versolato, O. O. Dependence of ion charge-energy emission from Nd:YAG-laser-produced plasma on laser intensity in the $0.4–40 \times 10^{10}$ W/cm^2 range. *Phys. Plasmas* **30**, 83505 (2023).
83. Totorica, S. R. et al. Acceleration mechanisms of energetic ion debris in laser-driven tin plasma EUV sources. *Appl. Phys. Lett.* **124**, 174101 (2024).
84. Fujioka, S. et al. Properties of ion debris emitted from laser-produced mass-limited tin plasmas for extreme ultraviolet light source applications. *Appl. Phys. Lett.* **87**, 241503 (2005).
85. Nakamura, D. et al. Mitigation of fast ions generated from laser-produced Sn plasma for extreme ultraviolet light source by H_2 gas. *J. Appl. Phys.* **102**, 123310 (2007).
86. Burdt, R. A. et al. Recombination effects during expansion into vacuum in laser produced Sn plasma. *Appl. Phys. Lett.* **97**, 41502 (2010).
87. Abramenko, D. B. et al. Measurements of hydrogen gas stopping efficiency for tin ions from laser-produced plasma. *Appl. Phys. Lett.* **112**, 164102 (2018).
88. Rai, S. et al. Charge exchange in collisions of 1–100-keV Sn^{3+} ions with H_2 and D_2. *Phys. Rev. A* **106**, 12804 (2022).
89. Rai, S. et al. Evidence of production of keV Sn^+ ions in the H_2 buffer gas surrounding an Sn-plasma EUV source. *Plasma Sources Sci. Technol.* **32**, 35006 (2023).
90. Bijlsma, K. et al. Electron capture from molecular hydrogen by metastable Sn^{2+*} Ions. *Atoms* **12**, 9 (2024).
91. Sheil, J. et al. Power-law scaling relating the average charge state and kinetic energy in expanding laser-driven plasmas. *Phys. Rev. Lett.* **133**, 125101 (2024).
92. Oltra, L. et al. Sequential synchronous mechanism for double-electron capture: insights into unforeseen large cross sections in low-energy $Sn^{3+} + H_2$ Collisions. *Phys. Rev. Lett.* **134**, 93002 (2025).
93. Liu, B. et al. Mass partitioning in fragmenting tin sheets. *Phys. Rev. Appl.* **20**, 14048 (2023).
94. Behnke, L. et al. High-energy parametric oscillator and amplifier pulsed light source at 2-μm. *Opt. Express* **31**, 24142–24156 (2023).
95. Ackermann, M. D., IJpes, D., Yakshin, A. E., Sturm, M. J. & Valpreda, A. Improving multilayers for maximum reflectivity. In *Optical and EUV Nanolithography XXXVIII*, vol. PC13424, PC134240F (SPIE, 2025).
96. Liu, K., Li, Y., Zhang, F. & Fan, M. Transient thermal and structural deformation and its impact on optical performance of projection optics for extreme ultraviolet lithography. *Jpn. J. Appl. Phys.* **46**, 6568 (2007).
97. Yang, G. & Li, Y. Analysis and control of thermal and structural deformation of projection optics for 22-nm EUV lithography. In *Extreme Ultrav. EUV Lithogr. III*, vol. 8322, 830–839 (SPIE, 2012).
98. Heays, A. N., Bosman, A. D. & van Dishoeck, E. F. Photodissociation and photoionisation of atoms and molecules of astrophysical interest. *Astron. Astrophys.* **602**, A105 (2017).
99. van der Horst, R. M. et al. Exploring the electron density in plasma induced by EUV radiation: I. Experimental study in hydrogen. *J. Phys. D: Appl. Phys.* **49**, 145203 (2016).
100. Basko, M. M., Novikov, V. G. & Grushin, A. S. On the structure of quasi-stationary laser ablation fronts in strongly radiating plasmas. *Phys. Plasmas* **22**, 53111 (2015).
101. Sheil, J., Versolato, O., Bakshi, V. & Scott, H. Review of the 1st EUV light sources code comparison workshop. *Atoms* **11**, 130 (2023).
102. Colombant, D. & Tonon, G. F. X-ray emission in laser-produced plasmas. *J. Appl. Phys.* **44**, 3524–3537 (1973).
103. Kawasaki, H. et al. Electron temperature and soft x-ray intensity scaling in laser heavy element plasma interaction. *AIP Adv.* **10**, 65306 (2020).
104. Wilhelm, R. A. et al. On the missing single collision peak in low energy heavy ion scattering. *Nucl. Instrum. Methods Phys. Res. B: Beam Interact. Mater.* **544**, 165123 (2023).
105. Murakami, M. & Basko, M. M. Self-similar expansion of finite-size non-quasi-neutral plasmas into vacuum: Relation to the problem of ion acceleration. *Phys. Plasmas* **13**, 12105 (2006).

106. Hemminga, D. J. et al. High-energy ions from Nd:YAG laser ablation of tin microdroplets: Comparison between experiment and a single-fluid hydrodynamic model. *Plasma Sources Sci. Technol.* **30**, 105006 (2021).
107. Dahmani, F. & Kerdja, T. Measurements and laser-wavelength dependence of mass-ablation rate and ablation pressure in planar layered targets. *Laser Part. Beams* **9**, 769–778 (1991).
108. Burdt, R. A. et al. Experimental scaling law for mass ablation rate from a Sn plasma generated by a 1064 nm laser. *J. Appl. Phys.* **106**, 33310 (2009).
109. Roudskoy, I. V. General features of highly charged ion generation in laser-produced plasmas. *Laser Part. Beams* **14**, 369–384 (1996).
110. Liu, B., Kurilovich, D., Gelderblom, H. & Versolato, O. O. Mass loss from a stretching semitransparent sheet of liquid tin. *Phys. Rev. Appl.* **13**, 24035 (2020).
111. Mostafa, Y., Behnke, L., Engels, D. J. & Versolato, O. O. Mass use in 2 μ m laser-driven tin plasma using sheet targets. *J. Appl. Phys.* **138**, 143304 (2025).
112. Kramida, A., Ralchenko, Y., Reader, J. & NIST ASD Team. NIST Atomic Spectra Database https://www.nist.gov/pml/atomic-spectra-database (2020).
113. O'Shay, B., Najmabadi, F., Harilal, S. S. & Tillack, M. S. Nanosecond spectroscopy of expanding laser-produced tin plasma. *J. Phys. Conf. Ser.* **59**, 773 (2007).
114. Tillack, M. S., Sequoia, K. L. & Tao, Y. Geometric effects on EUV emissions in spherical and planar targets. *J. Phys. Conf. Ser.* **112**, 42060 (2008).
115. Sizyuk, T. & Hassanein, A. Tuning laser wavelength and pulse duration to improve the conversion efficiency and performance of EUV sources for nanolithography. *Phys. Plasmas* **27**, 103507 (2020).
116. Basko, M. M. On the maximum conversion efficiency into the 13.5-nm extreme ultraviolet emission under a steady-state laser ablation of tin microspheres. *Phys. Plasmas* **23**, 83114 (2016).
117. Burkhalter, P. G., Feldman, U. & Cowan, R. D. Transitions in highly ionized Sn spectra from a laser-produced plasma. *J. Opt. Soc. Am.* **64**, 1058–1062 (1974).
118. Khan, M. A. Spectra of Sn xx–Sn xxii in the extreme ultraviolet. *J. Opt. Soc. Am.* **72**, 268–272 (1982).
119. Wyart, J.-F., Mandelbaum, P., Klapisch, M., Schwob, J.-L. & Schweitzer, N. Identification of $n = 5$ to $n = 4$ transitions in zinc-like ions from yttrium to tin (Y X-Sn XXI). *Phys. Scr.* **36**, 224 (1987).
120. Chung, H.-K., Chen, M. H., Morgan, W. L., Ralchenko, Y. & Lee, R. W. FLYCHK: Generalized population kinetics and spectral model for rapid spectroscopic analysis for all elements. *High. Energy Density Phys.* **1**, 3–12 (2005).
121. Ciricosta, O. et al. Direct measurements of the ionization potential depression in a dense plasma. *Phys. Rev. Lett.* **109**, 065002 (2012).
122. Badnell, N. R. et al. Dielectronic recombination of heavy species: The tin $4p^64d^q - 4p^64d^{(q-1)}4f + 4p^54d^{(q+1)}$ transition arrays for q = 1–10. *J. Phys. B:. Mol. Opt. Phys.* **44**, 135201 (2011).
123. Assink, L. et al. The voltage dependent transmission function of a retarding field analyzer. *Nucl. Instrum. Methods. Phys. Res., Sect B* **579**, 166217 (2026).
124. Engels, D. J. et al. High-resolution spectroscopic imaging of atoms and nanoparticles in thin film vaporization. *Appl. Phys. Lett.* **123**, 254102 (2023).

Acknowledgements

The authors thank Stan de Lange and Jorge Gonzalez for valuable discussions and ASML for loaning the Horizon OPO laser system. We would also like to thank Henk-Jan Boluijt and Laurens van Buuren for their work on the experimental setup and Jorijn Kuster for his work on the acquisition software.

Author contributions

D.J.E., F.M.K. and Y.M. set up and performed the experiments, with contributions from E.J.S. Data analysis was performed by D.J.E., F.M.K., Y.M. and B.S. The project was supervised by O.O.V., with contributions from R.H., J.S. and W.U. All authors discussed the results and contributed to the writing of the paper.

Funding

This work was conducted at the Advanced Research Center for Nanolithography (ARCNL), a public-private partnership between the University of Amsterdam (UvA), Vrije Universiteit Amsterdam (VU), Rijksuniversiteit Groningen (UG), the Dutch Research Council (NWO), and the semiconductor equipment manufacturer ASML and was partly financed by 'Toeslag voor Topconsortia voor Kennis en Innovatie (TKI)' from the Dutch Ministry of Economic Affairs and Climate Policy and the European Research Council (ERC StG Project no. 802648 and CoG Project no. 101086839). This publication is also a part of the project 'Plasma driven by a variable-wavelength laser for next-generation EUV sources for nanolithography' (with project number 19458) of the Open Technology Programme, which is financed by NWO.

Competing interests

The authors declare no competing interests.

Additional information

Correspondence and requests for materials should be addressed to O. O. Versolato.

Peer review information *Communications Physics* thanks the anonymous reviewers for their contribution to the peer review of this work

Reprints and permissions information is available at http://www.nature.com/reprints

Publisher's note Springer Nature remains neutral with regard to jurisdictional claims in published maps and institutional affiliations.

Open Access This article is licensed under a Creative Commons Attribution-NonCommercial-NoDerivatives 4.0 International License, which permits any non-commercial use, sharing, distribution and reproduction in any medium or format, as long as you give appropriate credit to the original author(s) and the source, provide a link to the Creative Commons licence, and indicate if you modified the licensed material. You do not have permission under this licence to share adapted material derived from this article or parts of it. The images or other third party material in this article are included in the article's Creative Commons licence, unless indicated otherwise in a credit line to the material. If material is not included in the article's Creative Commons licence and your intended use is not permitted by statutory regulation or exceeds the permitted use, you will need to obtain permission directly from the copyright holder. To view a copy of this licence, visit http://creativecommons.org/licenses/by-nc-nd/4.0/.

© The Author(s) 2026